



Original article

Numerical simulation of power-law acid flow in rough fractures of carbonate rocks

Xu Liu^{1,2}, Qin Li^{1,2}, Wenling Chen^{1,2}, Na Li^{1,2}, Yan Huang³, Huazhou Li⁴

¹College of Energy, Chengdu University of Technology, Chengdu 610059, P. R. China

²State Key Laboratory of Oil and Gas Reservoir Geology and Exploitation, Chengdu University of Technology, Chengdu 610059, P. R. China

³Zhundong Drilling Company of CNPC Xibu Drilling Engineering Co., Ltd., Urumqi 834000, P. R. China

⁴School of Mining and Petroleum Engineering, Faculty of Engineering, University of Alberta, Edmonton T6G 1H9, Canada

Keywords:

Acid fracturing
acid-rock reaction
rheological property
rough fracture
numerical simulation

Cited as:

Liu, X., Li, Q., Chen, W., Li, N., Huang, Y., Li, H. Numerical simulation of power-law acid flow in rough fractures of carbonate rocks. *Advances in Geo-Energy Research*, 2025, 17(3): 226-240.
<https://doi.org/10.46690/ager.2025.09.05>

Abstract:

Acid fracturing is the most widely applied technology for stimulating carbonate reservoirs. Meanwhile, the effectiveness of this method largely depends on factors such as acid penetration distance, fracture morphology and conductivity, all of which are closely governed by acid flow behavior. A wealth of numerical simulations have been conducted to characterize acid flow during fracturing, whereas the coupled effects of acid rheological properties and fracture surface roughness on the acid flow behavior remain underexplored. In this work, a three-dimensional numerical model of acid etching fracture was developed by coupling an acid-rock reaction model with computational fluid dynamics methods, which comprehensively incorporates the rheological property of acid and fracture surface roughness. Validation against experimental data showed a deviation of 11.15% in dissolved mass, with errors within 10.00% for most roughness parameters, confirming the numerical model's accuracy. Furthermore, the numerical model was employed to investigate the quantitative effect of the rheological index on acid transport and the spatiotemporal evolution of acid flow and dissolution. The results revealed significant interdependencies among flow velocity, shear rate, acid-rock reaction rate, and fracture width, all of which evolve dynamically over time and space. Moreover, it was found that the non-uniform distribution of flow velocity, shear rate, acid-rock reaction rate is caused by fracture surface roughness, and the degree of non-uniformity is enhanced as the shear-thinning capacity of the acid increases. This work provides a robust numerical framework for the simulation of the transport and reaction of acids with power-law characteristics in three-dimensional rough fractures, thus offers valuable theoretical insights for guiding the optimization of acid fracturing parameters and enhancing reservoir stimulation efficiency.

1. Introduction

Carbonate reservoirs hold more than 70% of oil and gas resources, making them extremely important energy sources (Deng et al., 2025; Karayel et al., 2022; Mehrabi et al., 2025). Acid fracturing is the most widely applied technology for stimulating carbonate reservoirs at present (Guo et al., 2020;

Ling et al., 2024; Zhao et al., 2024). The key to its successful stimulation is the non-uniform etching of fracture surfaces by acid, forming flow channels with high conductivity (Al-Shargabi et al., 2023; Liu et al., 2024; Liu et al., 2025b). Acid flow in fractures directly affects the acid-etched morphology and conductivity of flow channels (Xu et al., 2023; Chen et al., 2024; Zeng and Zhou, 2025), which is of great importance

to the effectiveness of acid fracturing.

In order to clarify the laws of acid flow in fractures, a large number of acid etching fracture models have been developed for carbonate reservoirs, which underwent an evolution from one-dimensional to three-dimensional (3D). Early models only reflected the one-dimensional steady-state flow and reaction of acid in fractures (Williams and Nierode, 1972; van Domselaar et al., 1973), while they provided an important foundation for the development of subsequent models. Later, the steady-state two-dimension models (Lo and Dean, 1989; Huang et al., 2020; Kotb et al., 2021), transient two-dimension (2D) models (Dong et al., 2002; Ugursal et al., 2019; Gou et al., 2021), pseudo-3D models (Romero et al., 2001; Alhubail et al., 2017; Aljawad et al., 2020), and full-3D models (Liu et al., 2023a; Barboza et al., 2022; Zhu et al., 2024) were developed. However, most of these models were based on ideal smooth fractures, and few incorporated the roughness of fracture surfaces. In fact, rough fracture surfaces cause the non-uniform distribution of the flow field in fractures and have a significant impact on acid flow (Lavrov, 2013; Ignatenko and Bryanskaya, 2023; Xu et al., 2024). Dong et al. (2002) incorporated fracture roughness and developed an acid etching fracture model for 2D flow along the length and height directions. Ugursal et al. (2019) integrated the *in-situ* stress field into the model developed by Dong et al. (2002) and simulated acid transport, acid-rock reaction, the fracture width increase resulting from fracture wall etching, and acid leakoff through natural fractures. Gou et al. (2021) improved the model developed by Dong et al. (2002) to simulate the dynamic coupling of acid flow, reactive transport and dissolution, and the mechanical deformation of asperities on the rough acid-etched fracture surface under normal closure stress. Although these 2D models consider the influence of fracture surface roughness, they still exhibit significant discrepancies from the 3D rough fractures in actual reservoirs. In our previous work, a 3D fracture model with real fracture surface roughness characteristics was developed through the “diamond-square” algorithm, and the acid-rock reaction rate model was coupled with the 3D fracture model to study the influence of fracture surface roughness, fracture width, and acid viscosity on the acid flow and reaction behavior. (Liu et al., 2025a). However, this model is only applicable to Newtonian acids and does not incorporate the influence of acid rheological properties.

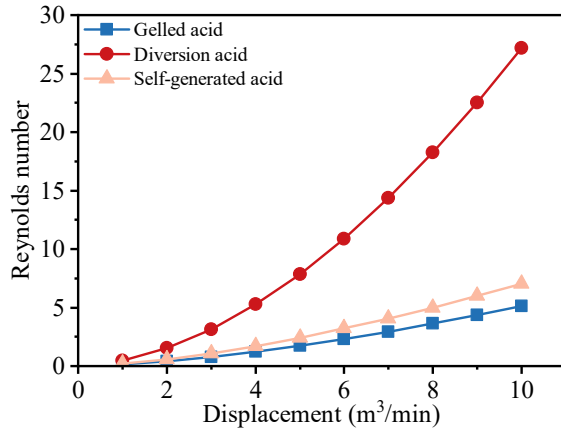
In acid fracturing operations in the field, it is common to add thickeners (such as gelled acid or crosslinked acid) to increase the viscosity of the acid, thereby achieving the goals of slowing down the acid-rock reaction rate and extending the effective acid penetration distance (Wang et al., 2022; Liu et al., 2023b; Zhang et al., 2025). The thickeners used are usually linear polymeric compounds with carbon-carbon chains as their main chains, which have a high relative molecular weight. In a shear flow field, its extended polymer chains entangle with each other and generate friction, significantly increasing fluid flow resistance and macroscopically manifesting as high system viscosity (Yu et al., 2021; Jiang et al., 2022; Sui et al., 2024). As the shear rate increases, the polymer chains gradually disentangle and even break. This causes the acid viscosity to decrease significantly, exhibiting obvious shear-

thinning behavior that matches the characteristics of power-law fluids (Li and Shi, 2022; Wang et al., 2024, 2025b). This phenomenon has a significant impact on the diffusion and mass transfer of H^+ (Abdelgawad et al., 2018; Subedi et al., 2020; Song and Lee, 2023), the acid-rock reaction rate (Maheshwari et al., 2016; Wang et al., 2018; Afsar et al., 2022) and the effective acid penetration distance (Zhao et al., 2020; Zhu et al., 2022; Kong et al., 2023). Romero et al. (2001) coupled the pseudo-3D hydraulic fracturing simulator with acid-rock reaction to develop a pseudo-3D acid etching fracture model suitable for power-law fluids. Their study found that the smaller the rheological index is, the higher the acid migration rate. Alhubail et al. (2017) utilized the finite element method and considered temperature and leak-off to develop a full 3D acid etching fracture model that is suitable for power-law fluids. They found that the penetration distance of pseudoplastic acid is shorter than Newtonian acid. Barboza et al. (2022) coupled the rheological model, reaction product migration model, and 3D acid etching model to establish an acid etching fracture model for self-diverting acid. Nonetheless, this model has difficulties in obtaining input parameters (such as shear rate and correction coefficients). Although these 3D models incorporate the influence of acid rheological properties, they still regard fractures as smooth plates and fail to consider the influence of fracture surface roughness. In fact, there are technical challenges in developing a numerical model for acid etching fractures with coupled flow, solid and chemical reactions within 3D rough fractures (Zhao et al., 2024). This is because the modeling of 3D rough fractures requires mesh refinement to capture the details of rough features, resulting in a sharp increase in the number of meshes (Wang et al., 2025a). If the calculation of the flow field and the chemical field is coupled, the calculation amount will increase exponentially, and the simulation is difficult to converge. To the best of the authors' knowledge, there have been few reports on the direct numerical simulation of acid flow in 3D rough fractures. Therefore, to more realistically simulate the flow and dissolution behavior of acid in fractures, it is necessary to develop a 3D acid etching fracture model that comprehensively incorporates fracture surface roughness and acid rheological properties based on our previous work (Liu et al., 2025a).

To address the above shortcomings, this study aimed to develop an acid etching fracture model for acid with power-law characteristics in 3D rough fractures and clarify the laws of acid flow in fractures during acid fracturing. The technical approach was as follows: Develop an acid-rock reaction rate model incorporating the rheological property based on boundary layer mass transfer theory; then, couple this acid-rock reaction rate model with computational fluid dynamics (CFD) method, and simulate the acid flow in 3D rough fractures through manual iteration. This work provides a robust numerical framework for simulating the transport and reaction of acids with power-law characteristics in 3D rough fractures, offering valuable theoretical insights for guiding the optimization of acid fracturing parameters and enhancing reservoir stimulation efficiency.

Table 1. Rheological parameters of acid fluid systems.

| Type | Rheological index | Consistency coefficient (Pa·s ⁿ) |
|----------------|-------------------|--|
| Gelled | 0.4489 | 7.8432 |
| Diversion | 0.2076 | 4.4460 |
| Self-generated | 0.4572 | 5.4899 |

**Fig. 1.** Reynolds numbers of acid fluid systems under different displacement rates.

2. Acid-rock reaction rate model

2.1 Acid flow regime

The acid flow regime directly affects the mass transfer efficiency of H^+ in fractures (Kumar et al., 2019; Haghani-Galougahi, 2021; Ivanishin et al., 2021). Therefore, it is vital to clarify the acid flow regime and thus accurately establish the acid-rock reaction model. First, according to the theory of non-Newtonian fluid flow, the modified Reynolds number of power-law fluids is defined as the dimensionless ratio of inertial forces to viscous forces (Bird et al., 2006):

$$Re = \frac{\rho u^{2-n} L^n}{\frac{K}{8} \left(\frac{6n+2}{n} \right)^n} \quad (1)$$

where Re represents the Reynolds number; ρ represents the acid density, kg/m³; u represents the acid flow velocity, m/s; L represents the fracture hydraulic diameter, m; n represents the rheological index (dimensionless, $0 < n < 1$); K represents the consistency coefficient, Pa·sⁿ.

Since the fracture width is much smaller than the fracture height, acid flow in the fracture can be regarded as 2D flow, and the hydraulic diameter can be approximated as follows:

$$L = 2w \quad (2)$$

where w represents the fracture width, m.

Considering the fracture as bilateral, the relationship between the acid flow velocity and displacement can be described as follows:

$$u = \frac{Q}{120wH} \quad (3)$$

where Q represents the acid pumping rate, m³/min; H represents the fracture height, m.

By integrating Eqs. (1)-(3), the formula for calculating the Reynolds number of power-law fluids in fractures can be derived as follows:

$$Re = \frac{\rho \left(\frac{Q}{120H} \right)^{2-n} w^{2n-2}}{\frac{K}{8} \left(\frac{3n+1}{n} \right)^n} \quad (4)$$

Rheological experiments on acid fluids at elevated temperatures (90 °C) were performed using a rotational rheometer. The rheological index and consistency coefficients of gelled acid, diversion acid, and self-generated acid were obtained (Table 1).

Assuming a fracture height of 50 m, a fracture width of 8 mm, and an acid density of 1,050 kg/m³, and by incorporating the acid rheological parameters, the Reynolds numbers of acid flow within the fracture under different displacement rates were calculated. The results showed that the flow Reynolds numbers of acid fluids during acid fracturing were all below 30 (Fig. 1). This finding indicates that acid fluids predominantly exhibit laminar flow within fractures. Subsequent investigations were all based on the assumption that the acid flow in fractures is fully developed laminar flow.

2.2 H^+ mass transfer rate

When acid flows along the fracture surface, the flow velocity near the wall is sharply reduced to zero due to the effect of viscous resistance, and a distinct velocity gradient region is formed. The thickness of this region is gradually increased as the flow develops, and a stable velocity boundary layer is finally formed at the fully developed stage. (Fig. A1). Meanwhile, during the migration of H^+ in the acid toward the rock surface, a concentration boundary layer is formed due to concentration differences (Nasr-El-Din et al., 2009; Peng et al., 2025). This layer is crossed by H^+ via diffusion. The H^+ mass transfer resistance is directly determined by the thickness of this layer, and the acid-rock reaction rate is influenced. By quantitatively solving the boundary layer thickness, the H^+ mass transfer coefficient and acid-rock reaction rate can be accurately determined.

Taking the micro-element control volume method (Fig. A2) and the law of mass conservation as bases, the integral mass transfer equation and the integral momentum equation are derived by calculating the mass inflow and outflow at each surface of the micro-element control volume, presented in Eqs. (5) and (6). The complete derivation process is detailed in Eqs. (S-1) to (S-12) in Appendix A of the Supplementary file:

$$\frac{\partial}{\partial x} \left[\int_0^{\delta_c} (C_0 - C) u_x dy \right] dx = D_H \frac{\partial C}{\partial y} \Big|_{y=0} \quad (5)$$

$$\rho \frac{d}{dx} \int_0^{\delta_v} (u_0 - u) u dy = \mu \frac{\partial u}{\partial y} \Big|_{y=0} \quad (6)$$

where C represents the H^+ concentration, mol/L; C_0 represents the H^+ concentration in the middle of the fracture, mol/L; D_H represents the H^+ diffusion coefficient, m^2/s ; u_0 represents the acid flow velocity in the middle of the fracture, m/s; δC represents the thickness of the concentration boundary layer, m; δV represents the thickness of the concentration velocity layer, m; μ represents the acid dynamic viscosity, Pa·s. The expressions of velocity distribution and concentration distribution in the boundary layer can be obtained by solving Eqs. (5) and (6) by the integral method. The complete derivation process is detailed in Eqs. (S-13) to (S-32) in Appendix A of the Supplementary file.

The H^+ mass transfer flux between the fracture surface and the fluid can be expressed as follows (Kadafur et al., 2020):

$$N_A = k(C_0 - C_w) \quad (7)$$

where N_A represents the mass transfer flux, $kmol/(m^2 \cdot s)$; k represents the mass transfer coefficient, m/s; C_w represents the H^+ concentration on the fracture surface, mol/L.

The H^+ mass transfer flux can be described in accordance with Fick's law as follows:

$$N_A = -D_H \left. \frac{dC}{dy} \right|_{y=0} = -D_H \left. \frac{d(C - C_w)}{dy} \right|_{y=0} \quad (8)$$

Eqs. (7) and (8) are solved simultaneously to obtain:

$$k = D_H \left. \frac{d \left[\frac{C_w - C}{C_0 - C_w} \right]}{dy} \right|_{y=0} \quad (9)$$

Combined with the mass transfer theory and the infinitesimal control volume method, the exact solution for the convective mass transfer coefficient of H^+ in the laminar boundary layer of the fracture can be determined. The complete derivation is presented in Eqs. (S-1) through (S-36). The local convective mass transfer coefficient at x from the fracture surface is given by the following expression:

$$k_x = 0.332 \frac{D_H}{x} Re^{1/2} Sc^{1/3} \quad (10)$$

where k_x represents the local mass transfer coefficient, m/s; x represents the vertical distance from the fracture surface, m; Sc represents the Schmidt number.

The convective mass transfer coefficient in fractures is given by:

$$k = \frac{1}{L} \int_0^L k_x dx = 0.664 \frac{D_H}{L} Re^{1/2} Sc^{1/3} \quad (11)$$

where L is the characteristic length, specifically the hydraulic diameter of the fluid flow within the fracture.

The Schmidt number is defined as the ratio of kinematic viscosity and diffusion coefficient:

$$Sc = \frac{\nu}{D_H} = \frac{\mu}{\rho D_H} \quad (12)$$

where ν represents the acid kinematic viscosity, m^2/s .

For power-law fluids, the apparent viscosity should be used in place of the dynamic viscosity characteristic of Newtonian fluids. The apparent viscosity is defined as the ratio of the

fluid's shear stress to its shear rate:

$$\mu_{app} = \frac{\tau}{\gamma} \quad (13)$$

where μ_{app} represents the acid apparent viscosity, Pa·s; τ represents the shear stress, Pa; γ represents the shear rate, s^{-1} .

The shear stress and shear rate of power-law fluids satisfy the following relationship:

$$\tau = K\gamma^n \quad (14)$$

By substituting Eqs. (13) and (14) into Eq. (12), the Schmidt number for power-law fluids can be derived as follows:

$$Sc = \frac{K}{\rho D_H} \gamma^{n-1} \quad (15)$$

By integrating Eqs. (1), (2), (11), and (15), the expression for the convective mass transfer coefficient of H^+ can be obtained.

$$k = 0.939 w^{(n-2)/2} u^{(2-n)/2} \gamma^{(n-1)/3} \left(\frac{3n+1}{n} \right)^{-n/2} \rho^{1/6} K^{-1/6} D_H^{2/3} \quad (16)$$

In high-temperature formations, the surface reaction of H^+ on the fracture surface proceeds at an extremely rapid rate, resulting in a very low concentration of H^+ at the fracture interface. The H^+ concentration on the fracture surface can be approximated as zero. By integrating Eqs. (7) and (16), the acid-rock reaction rate equation governed by mass transfer control can thus be derived:

$$J_A = 0.1 N_A = 0.0939 w^{(n-2)/2} u^{(2-n)/2} \gamma^{(n-1)/3} \left(\frac{3n+1}{n} \right)^{-n/2} \rho^{1/6} K^{-1/6} D_H^{2/3} C_0 \quad (17)$$

where J_A represents the acid-rock reaction rate, $mol/(cm^2 \cdot s)$.

By integrating the revised formula for the diffusion coefficient in infinitely dilute solutions, the formula for the H^+ diffusion coefficient under different temperatures and acid concentrations is derived as follows (Li et al., 2016):

$$D_H = \frac{9.77 \times 10^{-11} e^{0.0847T} C_0 + 1.61 \times 10^{-9} e^{0.0237T}}{1000 \mu_{app}} \quad (18)$$

where T represents the formation temperature, $^{\circ}C$.

By integrating Eqs. (13), (14), (17), and (18), the acid-rock reaction rate equation can be derived as follows:

$$J_A = 0.000939 w^{\frac{n-2}{2}} u^{\frac{2-n}{2}} \gamma^{\frac{1-n}{3}} \left(\frac{3n+1}{n} \right)^{\frac{n}{2}} \rho^{\frac{1}{6}} K^{-\frac{1}{6}} C_0 \left(9.77 \times 10^{-11} e^{0.0847T} C_0 + 1.61 \times 10^{-9} e^{0.0237T} \right)^{\frac{2}{3}} \quad (19)$$

This acid-rock reaction rate model incorporates the parameters of fracture width, acid flow velocity, acid shear rate, acid density, acid concentration, formation temperature, and acid rheological properties, making it applicable for calculating the mass transfer-controlled acid-rock reaction rate during linear acid flow.

3. Numerical model

3.1 Governing equation

The Fluent software was employed in this study to conduct numerical simulations of the acid flow behavior in 3D rough fractures. The analytical solution of fluid flow within a 3D model entails a complex process of solving the Navier-Stokes equations. To simplify the solving process, the following conditions need to be assumed:

- 1) The heat produced by the acid-rock reaction and the heat exchange between the formation and the acid fluid are not considered.
- 2) The filtration loss of the acid fluid on the fracture surface is not considered.
- 3) No deformation occurs throughout the entire model.
- 4) The simulation concentrates on the flow of acid in fractures during the injection process, specifically when the fractures are in an open state.

Fluid flow fundamentally follows the principles of conservation of mass, conservation of momentum, and conservation of energy. Since the fluid flow examined in this study does not entail energy exchange, the behavior of acid flow herein is governed solely by the conservation of mass and conservation of momentum.

The equation representing the conservation of mass can be formulated as follows:

$$\frac{\partial \rho}{\partial t} + \frac{\partial(\rho u_x)}{\partial x} + \frac{\partial(\rho u_y)}{\partial y} + \frac{\partial(\rho u_z)}{\partial z} = 0 \quad (20)$$

where u_x , u_y and u_z correspond to the velocities in the x , y , and z directions, respectively; t denotes time, s.

Next, the Hamiltonian differential operator is introduced:

$$\nabla = \mathbf{i} \frac{\partial}{\partial x} + \mathbf{j} \frac{\partial}{\partial y} + \mathbf{k} \frac{\partial}{\partial z} \quad (21)$$

Then, Eq. (20) can be expressed as follows:

$$\frac{\partial \rho}{\partial t} + \nabla \cdot (\rho \mathbf{u}) = 0 \quad (22)$$

According to Newton's second law, the momentum equations for the x , y , and z directions can be derived as follows:

$$\frac{\partial(\rho u_x)}{\partial t} + \nabla \cdot (\rho u_x \mathbf{u}) = -\frac{\partial p}{\partial x} + \frac{\partial \tau_{xx}}{\partial x} + \frac{\partial \tau_{yx}}{\partial y} + \frac{\partial \tau_{zx}}{\partial z} + \rho f_x \quad (23)$$

$$\frac{\partial(\rho u_y)}{\partial t} + \nabla \cdot (\rho u_y \mathbf{u}) = -\frac{\partial p}{\partial y} + \frac{\partial \tau_{xy}}{\partial x} + \frac{\partial \tau_{yy}}{\partial y} + \frac{\partial \tau_{zy}}{\partial z} + \rho f_y \quad (24)$$

$$\frac{\partial(\rho u_z)}{\partial t} + \nabla \cdot (\rho u_z \mathbf{u}) = -\frac{\partial p}{\partial z} + \frac{\partial \tau_{xz}}{\partial x} + \frac{\partial \tau_{yz}}{\partial y} + \frac{\partial \tau_{zz}}{\partial z} + \rho f_z \quad (25)$$

where P represents the pressure on the fluid elemental volume, Pa; τ_{xx} , τ_{xy} and τ_{xz} are the components of the viscous stress arising from molecular viscosity and acting on the surface of the fluid elemental volume, Pa; f_x , f_y and f_z are the force per unit mass in three directions, m/s^2 .

The finite volume method was employed to derive discrete equation grounded in the principle of momentum conservation. The 3D convection-diffusion conservation differential equation is represented as follows:

$$\begin{aligned} & \frac{\partial(\rho \phi)}{\partial t} + \frac{\partial(\rho u \phi)}{\partial x} + \frac{\partial(\rho v \phi)}{\partial y} + \frac{\partial(\rho w \phi)}{\partial z} \\ &= \frac{\partial}{\partial x} \left(D_H \frac{\partial \phi}{\partial x} \right) + \frac{\partial}{\partial y} \left(D_H \frac{\partial \phi}{\partial y} \right) + \frac{\partial}{\partial z} \left(D_H \frac{\partial \phi}{\partial z} \right) + S_\phi \end{aligned} \quad (26)$$

where ϕ represents the convective-diffusive substance function; S_ϕ represents the source item. Then, Eq. (26) can be expressed as:

$$\frac{\partial}{\partial t}(\rho \phi) + \text{div}(\rho \mathbf{u} \phi) = \text{div}(K \text{grad} \phi) + S_\phi \quad (27)$$

Subsequently, the governing equations are integrated:

$$\begin{aligned} & \int_{CV} \left[\int_t^{t+\Delta t} \frac{\partial}{\partial t}(\rho \phi) dt \right] dV + \int_t^{t+\Delta t} \left[\int_A \mathbf{n} \cdot (\rho \mathbf{u} \phi) dA \right] dt \\ &= \int_t^{t+\Delta t} \left[\int_A \mathbf{n} \cdot (K \nabla \phi) dA \right] dt + \int_t^{t+\Delta t} \int_{CV} S_\phi dV dt \end{aligned} \quad (28)$$

To solve these governing equations, three segregated solvers (SIMPLE, SIMPLER, and PISO) are provided in Fluent. Among these, the SIMPLE algorithm is easy to converge, while it has the disadvantage of high computational load. The SIMPLER algorithm is faster to converge, but this also has the disadvantage of high computational load. The PISO algorithm has a shorter iteration time, but the overall calculation time takes longer. Considering the simulation conditions and model characteristics, this study comprehensively evaluated the advantages, limitations and applicable scopes of these algorithms, and selected the SIMPLE algorithm to solve the 3D Navier-Stokes equations for fluid flow in rough fractures.

3.2 Modeling process

A fluid-solid coupling study on acid flow in 3D fractures was conducted based on the rough fracture geometric model established from a real core. The modeling process of the fluid-solid coupling numerical model is as follows (Fig. 2):

- Step 1: The standard rock pillar with a diameter of 45 mm and a height of 50 mm is split by a Brazilian splitting instrument to generate penetrating artificial fractures with natural roughness characteristics.
- Step 2: The entire fracture surface is scanned by a high-precision 3D laser scanner with a scanning accuracy of 0.05 mm, and the 3D coordinate data of the fracture is obtained.
- Step 3: The original point cloud data is processed (such as denoising, stitching and simplification) by the Geomagic Studio point cloud processing software to remove redundant and noise points. The 3D geometric model of the fracture surface is generated through surface processing, thereby enabling the transformation of the fracture morphology from a physical entity into a digital model.
- Step 4: The 3D fracture model is imported into the mesh generation software. Mesh refinement is performed on key areas (such as fracture walls) using adaptive mesh generation technology, so as to balance computational accuracy and computational efficiency. Using this method, high-quality computational meshes are created

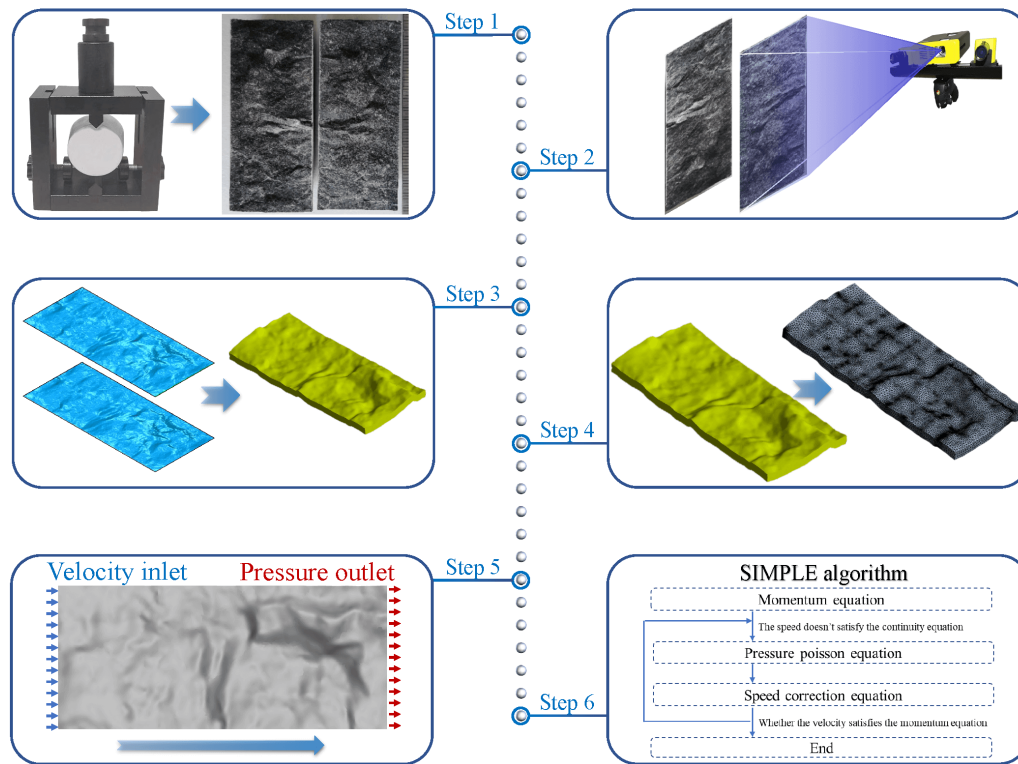


Fig. 2. Flowchart for developing the numerical model.

to accurately represent the fracture morphology.

- Step 5: The mesh model is imported into Fluent software, where the boundary conditions are established as velocity inlet and pressure outlet, and the properties of the acidic fluid are concurrently defined.
- Step 6: The SIMPLE algorithm is employed to sequentially solve the momentum equation, pressure Poisson equation, velocity correction equation, and related equations. During the iterative process, the velocity field is evaluated to ensure that it satisfies the momentum equation, thereby guaranteeing computational convergence. This solution method facilitates the simulation of acidic fluid flow behavior within fractures and provides numerical results, including the distribution of velocity and shear rate within the fractures.

After developing the fluid-solid coupling numerical model of 3D rough fractures, the acid-rock reaction rate model is coupled, and the flow and reaction behavior of acid in rough fractures can be simulated by manual iteration. The simulation steps are as follows: Firstly, the flow field distribution characteristics (such as velocity distribution and shear rate distribution) of acid in the initial fracture are obtained by CFD simulation. Secondly, on the basis of the flow field distribution, the chemical field distribution characteristics (such as reaction rate distribution and dissolution width distribution) of the acid are calculated by combining the acid-rock reaction rate model, and the coordinate parameters of acid-etched fracture surface after a certain time step are obtained. Thirdly, by remodeling the acid-etched fracture and repeating the above steps, the dy-

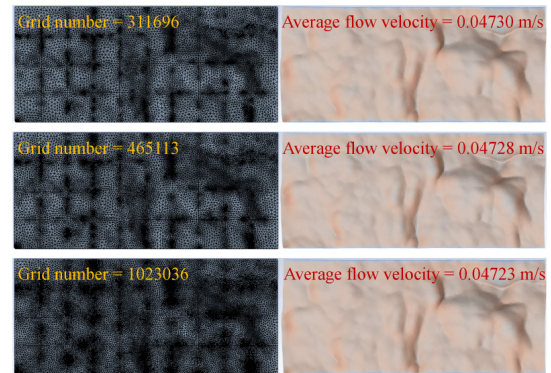


Fig. 3. Grid independence verification results.

namic evolution process of acid flow and reaction in the 3D rough fracture can be simulated.

3.3 Grid independence verification

In order to reduce the impact of mesh density on numerical simulation results and achieve an optimal balance between computational accuracy and efficiency, three different mesh densities are adopted. Consistent boundary conditions and simulation time steps are used for all simulations.

The simulation results show that the flow velocity contour clouds under different mesh densities exhibit a consistent distribution pattern. In order to perform quantitative validation, the average flow velocity of acid at the midpoint of the fracture is calculated for three different mesh configurations, yielding values of 0.04730, 0.04728 and 0.04723 m/s, respectively, with the errors all below 1.00% (Fig. 3). The grid independence of

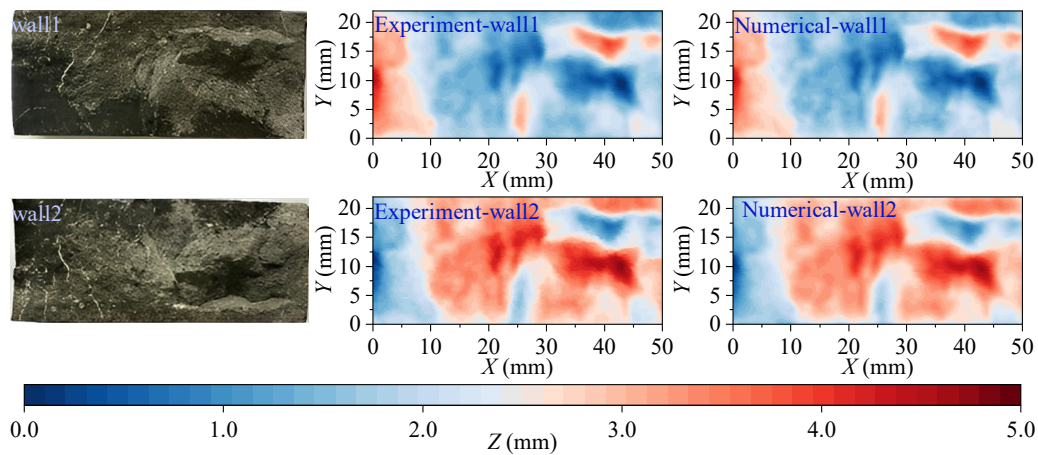


Fig. 4. Contour maps of fracture surface morphology from the experiment and numerical simulation.

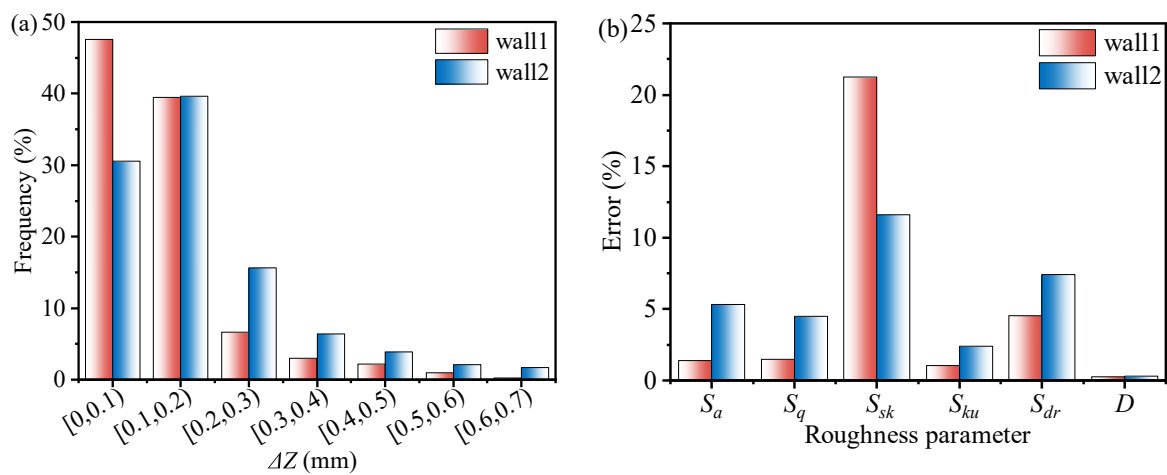


Fig. 5. Comparison of fracture surface morphology parameters between experiment and numerical simulation: (a) Fracture surface height difference, and (b) roughness parameters.

the numerical model is verified and the mesh configuration consisting of 465,113 elements is adopted for subsequent simulations to optimize the balance between computational accuracy and efficiency.

4. Experimental verification

In order to verify the accuracy of the numerical model, an acid flow reaction experiment was conducted by an acidizing conductivity tester, and the dissolution mass and dissolution morphology of the sample were calculated by numerical simulation and compared with the experimental data. The details of the experiment can be found in Appendix B of the supplementary file. The acid in the experiment was gelled acid, whose rheological properties are characterized by rheological testing, yielding a consistency coefficient (K) of 7.8432 and a rheological index (n) of 0.4489. The following experimental conditions were maintained: Temperature of 90 °C, acid injection velocity of 0.04 m/s, injection duration of 5 min, and initial fracture width of 2 mm, ensuring consistency between the experimental and simulation parameters.

The experimentally determined dissolution mass of the rock sample was 3.14 g, while a dissolution mass of 2.79 g was predicted by the numerical simulation, corresponding to an error margin of 11.15%. The rock samples after the experiment were scanned to obtain the fracture surface morphology and compare the experimental and numerical simulation results (Fig. 4).

The differences in fracture surface height and roughness parameters between experimental results and numerical simulation results were further compared. It is shown that the fracture surface height differences were mainly in the range of 0-0.3 mm, among which the proportions of wall1 and wall2 were 93.64% and 85.84%, respectively (Fig. 5(a)). To quantitatively characterize the changes in fracture surface roughness, the arithmetic mean height (S_a), root mean square height (S_q), skewness (S_{sk}), kurtosis (S_{ku}), surface development ratio (S_{dr}), and fractal dimension (D) were selected as evaluation parameters, which are defined by the international standard ISO 25178. The height amplitude, distribution pattern and spatial structure characteristics of the fracture surface are covered by these parameters. Thereby, the fracture surface

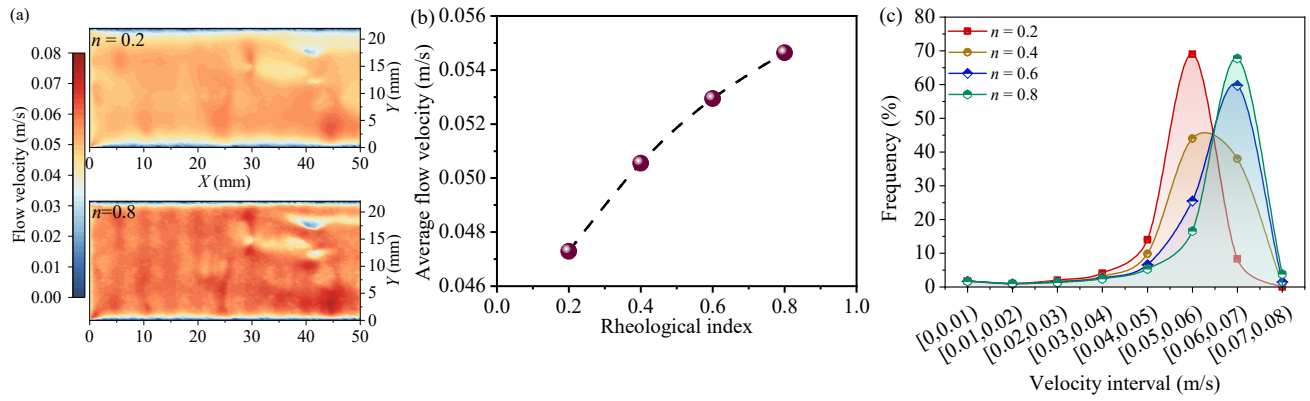


Fig. 6. Distribution of acid flow velocity in the middle of the fracture under different rheological indices: (a) Contour map of velocity distribution, (b) average velocity and (c) distribution frequency of velocity intervals.

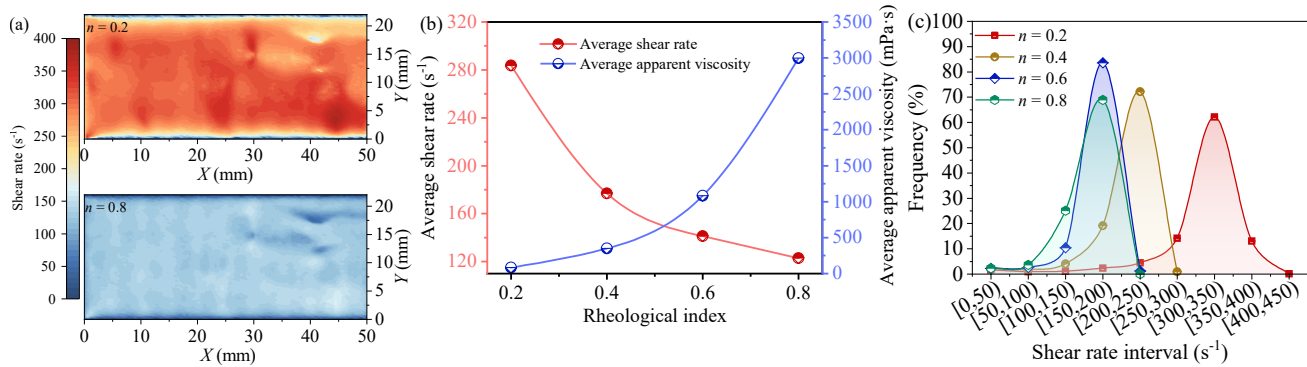


Fig. 7. Distribution of acid shear rate under different rheological indices: (a) Contour map of shear rate distribution, (b) average shear rate and apparent viscosity and (c) distribution frequency of shear rate intervals.

roughness could be comprehensively and accurately characterized. The computational methods for these parameters are detailed in Eqs. (S-46) to (S-54) in Appendix C of the supplementary file. The errors of fracture surface roughness parameters (including S_a , S_q , S_{ku} , S_{dr} , and D) were all below 10.00%, while the error of S_{sk} was in the range of 10.00%-20.00% (Fig. 5(b)). The relatively larger error of S_{sk} may be attributed to shadow effects or noise encountered by the laser scanner when scanning steep sidewalls or deep, narrow grooves. The underestimation or smoothing of extreme values are caused by these factors. Overall, the experimental results and numerical simulation results were in good agreement, and the accuracy of the numerical simulation was verified.

5. Results and discussion

5.1 Effect of rheological index

In order to clarify the influence of the shear thinning property of acid on its flow and reaction in fractures, the flow and dissolution behaviors of acid under different rheological indices ($n = 0.2, 0.4, 0.6, 0.8$) were simulated. The numerical simulation parameters were defined as follows: Injection velocity of 0.04 m/s, acid fluid consistency coefficient of 7.8432, acid fluid density of 1,050 kg/m³, acid concentration of 6 mol/L, formation temperature of 90 °C, initial fracture width of 2 mm, and an injection duration of 5 min.

After simulating with the CFD method, the distributions of acid flow velocity and shear rate in the middle of the fracture were obtained (Figs. 6-7). The results show that as n increases, the average flow velocity exhibits a non-linear monotonically increasing trend, while the rate of increase is gradually reduced (Figs. 6(a)-6(b)). Specifically, as n increases from 0.2 to 0.8, the relative growth rates of the average flow velocity are 6.90%, 4.70% and 3.20%, respectively. When $n = 0.2$, the flow velocity is predominantly distributed in the range of 0.05-0.06 m/s, accounting for 68.96%, while the proportion of flow velocity exceeding 0.06 m/s is only 8.30%. As n increases, the primary flow velocity interval shifts from 0.05-0.06 to 0.06-0.07 m/s. When $n = 0.8$, the proportion of flow velocity greater than 0.06 m/s rises to 71.65% (Fig. 6(c)).

It could be found that the average shear rate of the acid is gradually reduced as n increases, whereas the magnitude of this decrease is correspondingly reduced, with reductions of 37.60%, 20.20% and 12.90% respectively. The average apparent viscosity increases exponentially (Figs. 7(a)-7(b)). The main shear rate range of the acid shifts downward as n increases, from 300-350 to 150-200 s^{-1} . Specifically, when $n = 0.2$, 61.25% of the distribution is accounted for by the 300-350 s^{-1} range, while only 8.07% is accounted for by the range below 200 s^{-1} ; when $n = 0.4$, 72.14% of the distribution is accounted for by the 200-250 s^{-1} range; when $n = 0.6$, 83.56% of the distribution is accounted for by the 150-200

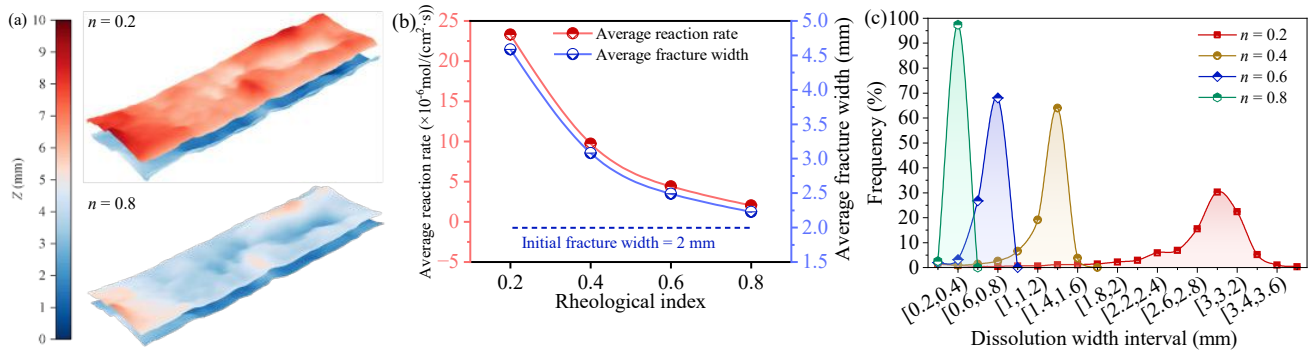


Fig. 8. Distribution of dissolution width under different rheological indices: (a) Contour map of fracture morphology, (b) average reaction rate and dissolution width and (c) distribution frequency of dissolution width intervals.

s^{-1} range; when $n = 0.8$, although the $150\text{--}200 \text{ s}^{-1}$ range still dominates, the proportion accounted for by the $100\text{--}150 \text{ s}^{-1}$ range is increased to 25.10% (Fig. 7(c)). This phenomenon is related to the shear thinning property of power-law acid. The acid with low rheological index is characterized by stronger shear thinning ability, which results in lower apparent viscosity and higher flow velocity exhibited by the acid under the same injection conditions, further resulting in the shear rate of the acid being enhanced.

When the data of acid flow velocity and shear rate in fractures are input into the acid-rock reaction rate model, the distribution of acid-rock reaction rate in fractures, dissolution width, and fracture surface morphology can be obtained. The average reaction rate, average fracture width after acid etching, and average dissolution width all show a significant exponential decreasing trend as n increases. Specifically, with each 0.2 increase in n , the average reaction rate is reduced by 53.60%–58.10%, and the average fracture width after acid etching is reduced by 10.50%–32.80%. The average dissolution width exhibits a trend similar to the average reaction rate (Fig. 8(a)–8(b)). The distribution of dissolution fracture width further indicates that the main distribution range of dissolution fracture width narrows as n increases. Specifically, when $n = 0.2$, the main distribution interval of dissolution width is 2.6–3.2 mm, accounting for 68.10%. With each 0.2 increase in n , this interval sequentially narrows to 1.0–1.4 (accounting for 83.10%), 0.4–0.8 (accounting for 94.80%), and 0.2–0.4 mm (accounting for 97.40%) (Fig. 8(c)). These data demonstrate that the stronger the shear thinning ability of the acid is, the stronger the non-uniform etching on the fracture surface.

The calculation of multidimensional roughness parameters reveals that the fracture surface roughness is increased after acid etching, whereas the extent of this increase progressively decreases with increasing n . Specifically, S_a and S_q show a consistent decreasing trend as n increases. For wall1, S_a and S_q decrease by 5.10% and 3.40% respectively; for wall2, the magnitude of the decrease in S_a and S_q is relatively larger, at 12.90% and 11.00% respectively (Figs. 9(a)–9(b)), which indicates a significant reduction in the average amplitude of surface undulations on the fracture. S_{sk} and S_{ku} gradually tend toward the unetched state as n increases (Figs. 9(c)–9(d)). S_{dr} is reduced from 0.1269 and 0.1325 when $n = 0.2$ to 0.0761 and

0.0759 when $n = 0.8$, with a reduction of more than 40.00% (Fig. 9(e)), which reflects a marked decrease in the spatial complexity of micro-protrusions on the fracture surface as n increases. D is gradually reduced from 2.6491 and 2.6545 when $n = 0.2$ to 2.6113 and 2.6128 when $n = 0.8$ (Fig. 9(f)), which indicates a substantial attenuation in the irregularity of the fracture surface profile as n increases. The reason for such changes in these roughness parameters is that when the shear thinning ability of the acid is strong, its apparent viscosity is low; when it flows in fractures, the mass transfer is uneven, which leads to local intense dissolution, and a rough surface with “high undulation and high complexity” is formed. As the shear thinning ability of the acid weakens, the apparent viscosity is increased, the reaction rate is reduced, the non-uniform etching ability is weakened, and the variation range of the roughness characteristics of the fracture surface is small.

Moreover, under the same rheological index, differences in the rough morphology of wall1 and wall2 are observed, and these differences increase as the shear thinning ability of the acid becomes stronger. For instance, when $n = 0.2$, the disparities in S_a , S_q , S_{sk} , S_{dr} , and D between wall2 and wall1 are 9.90%, 8.90%, 21.10%, 4.40%, and 0.0054, respectively; when $n = 0.8$, these differences diminish to 0.70%, 0.50%, 3.20%, 0.80%, and 0.0015, respectively. It can be seen that the enhanced shear thinning ability of the acid facilitates non-uniform etching in fractures.

5.2 Dynamic process of acid flow and reaction

In order to clarify the dynamic evolution law of acid flow and reaction in fractures, the flow and dissolution behaviors of acid in fractures under different acid injection durations (0 ~ 5, 5 ~ 10, 10 ~ 15, and 15 ~ 20 min) were simulated by manual iteration. The numerical simulation parameters are defined as follows: The acid injection time step of 5 min, injection velocity of 0.04 m/s, acid rheological index of 0.2, acid consistency coefficient of 7.8432, acid density of 1,050 kg/m^3 , acid concentration of 6 mol/L, formation temperature of 90 °C, and an initial fracture width of 2 mm.

The simulation results demonstrate that the flow and dissolution behaviors of the acid in fractures exhibit a spatiotemporal evolution law (Fig. 10). At the early stage of acid injection, an obvious velocity gradient between the fracture center and

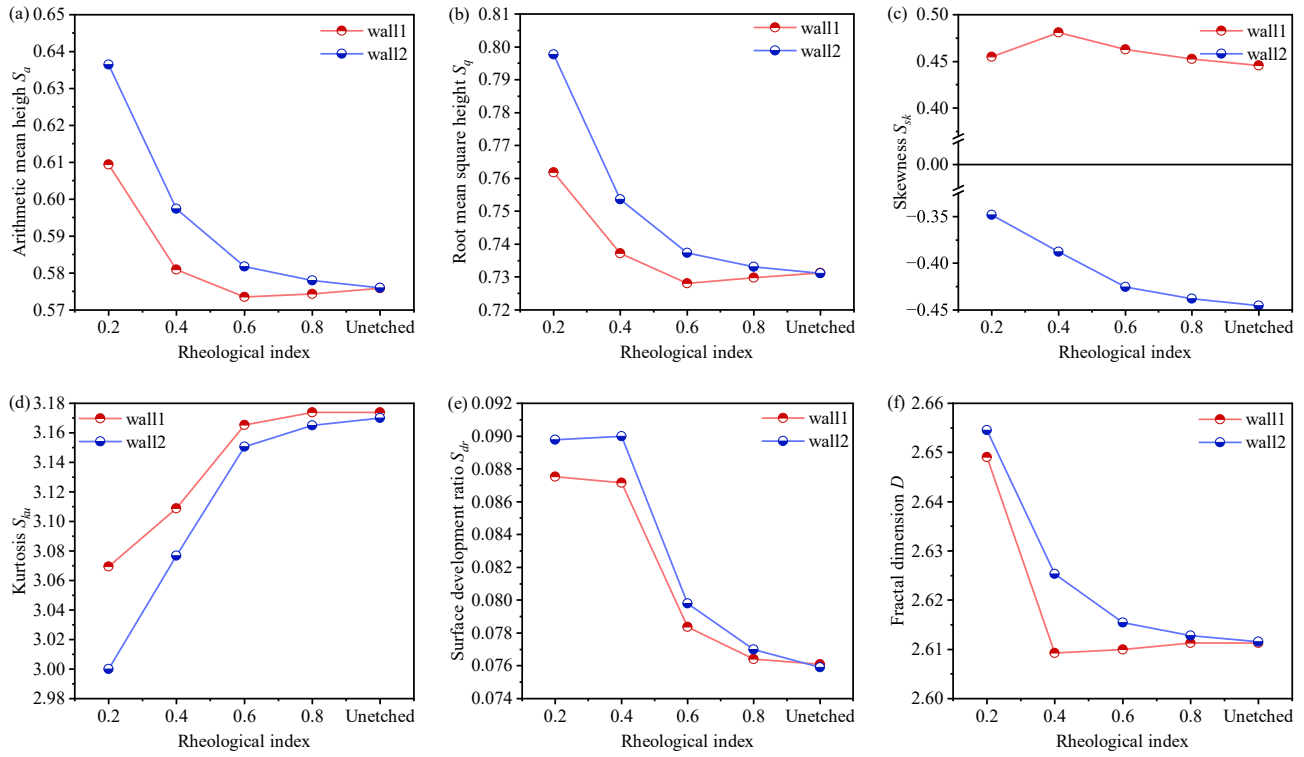


Fig. 9. Roughness parameters of acid-etched fracture surfaces under different rheological indices: (a) Arithmetic mean height S_a , (b) root mean square height S_q , (c) skewness S_{sk} , (d) kurtosis S_{ku} , (e) surface development ratio S_{dr} and (f) fractal dimension D .

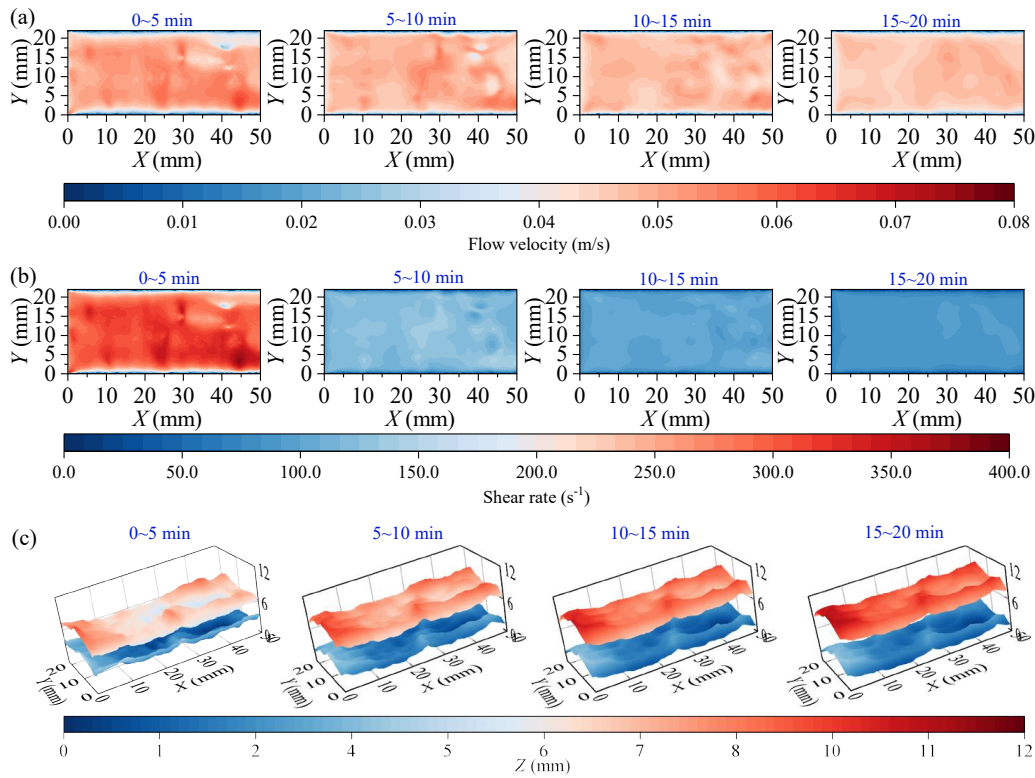
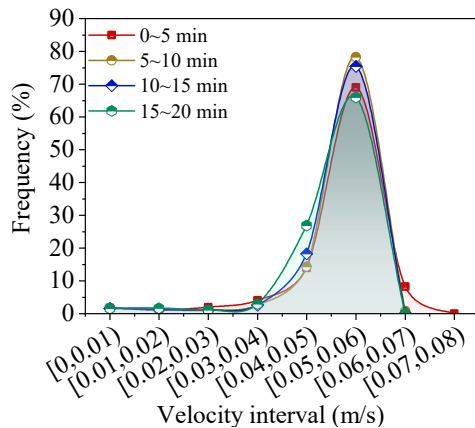


Fig. 10. Flow characteristics and fracture morphology changes during the acid flow reaction process: (a) Velocity distribution, (b) shear rate distribution and (c) fracture morphology.

Table 2. Average flow velocity of acid.

| Period (min) | Velocity (m/s) |
|--------------|----------------|
| 0 ~ 5 | 0.04728 |
| 5 ~ 10 | 0.04583 |
| 10 ~ 15 | 0.04497 |
| 15 ~ 20 | 0.04372 |

**Fig. 11.** Distribution law of flow velocity under different acid injection periods.

its wall surfaces is formed because of the relatively narrow fracture width. A high shear rate is imparted to the acid by this gradient, resulting in low viscosity. The acid-rock reaction rate is then accelerated, causing the fracture width to be rapidly increased. With the increase in fracture width, the velocity difference between the fracture center and its walls is reduced. This reduction causes the shear rate to be decreased, resulting in the apparent viscosity of the acid being increased. The acid-rock reaction rate is thus reduced, and the rate of fracture width increase is slowed down.

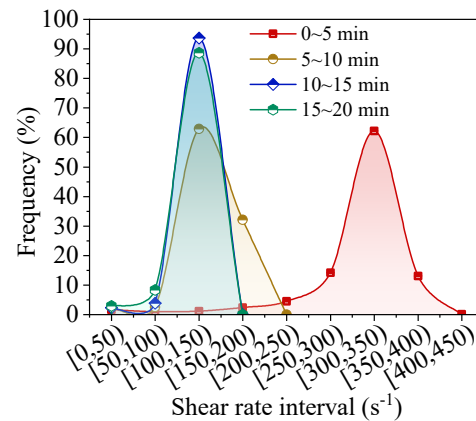
The average flow velocity of acid at the middle of the fracture over various time intervals is presented in Table 2. As the injection time progresses, the average flow rate is shown a consistent decreasing trend. The percentage decreases in flow velocity for the time intervals 0 ~ 5, 5 ~ 10, and 15 ~ 20 min are 3.08%, 1.87%, and 2.77%, respectively.

The analysis of flow velocity distribution (Fig. 11) shows that, although the main interval remains consistently within 0.05–0.06 m/s during acid injection, the proportion of this interval is gradually reduced as dissolution progresses. Specifically, the flow velocity interval of 0.06–0.07 m/s is only observed in the initial injection stage, accounting for 8.30%. As the injection time progresses, the proportion of the 0.05–0.06 m/s is decreased from 78.22% to 65.96%, whereas the proportion of the 0.04–0.05 m/s is correspondingly increased from 14.34% to 26.87%.

The average shear rate and apparent viscosity of the acid under varying acid injection intervals are presented in Table 3. The fitting results indicate that as the injection time progresses, the average shear rate decrease exponentially, with the corre-

Table 3. Average shear rate and apparent viscosity of acid.

| Period (min) | Shear rate (s^{-1}) | Apparent viscosity (mPa·s) |
|--------------|-------------------------|----------------------------|
| 0 ~ 5 | 283.71 | 85.55 |
| 5 ~ 10 | 117.01 | 173.75 |
| 10 ~ 15 | 96.02 | 203.51 |
| 15 ~ 20 | 82.89 | 228.92 |

**Fig. 12.** Distribution law of shear rate under different acid injection periods.

sponding percentage decreases found to be 58.76%, 17.93% and 13.68% respectively. Conversely, the average apparent viscosity increases logarithmically, with the respective percentage increases found to be 103.11%, 17.13% and 12.49%.

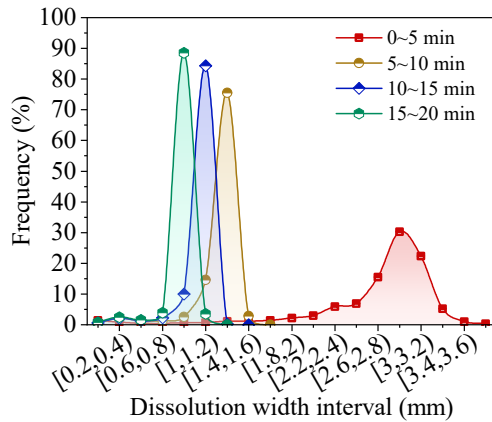
The analysis of the shear rates distribution (Fig. 12) shows that, at the early stage of acid injection, the shear rate is relatively high and is mainly concentrated in the interval of 300–350 s^{-1} , accounting for 62.15%. As the acid injection time is increased to the 5 ~ 10 min stage, the distribution interval of the shear rate is decreased to 100–200 s^{-1} , representing 94.99%. When the acid injection time is further increased, the shear rate is mainly distributed in the interval of 100–150 s^{-1} , with the corresponding proportions being 93.72% and 88.67%, respectively, and the difference between these proportions is gradually diminished.

The average reaction rate and average fracture width of acid under varying acid injection intervals are presented in Table 4. The fitting results indicate that as the injection time progresses, the average reaction rate decreases exponentially, with the corresponding percentage decreases found to be 64.46%, 20.63%, and 15.73% respectively. Conversely, the average fracture width increases logarithmically, with the respective percentage increases found to be 129.37%, 22.50%, 12.99%, and 9.37%.

The analysis of distributions of the dissolution widths (Fig. 13) shows that the distribution range of dissolution widths is relatively wide in the early stage of acid injection. Due to the relatively high acid-rock reaction rate, the fracture width is expanded rapidly, and the main increase is concentrated in the range of 2.6–3.2 mm, accounting for 68.10%. As dissolution

Table 4. Average reaction rate of acid and fracture width.

| Period (min) | Reaction rate ($\times 10^{-6}$ mol/(cm ² ·s)) | Fracture width (mm) |
|--------------|---|------------------------|
| 0 ~ 5 | 23.29 | 4.59 |
| 5 ~ 10 | 8.28 | 5.62 |
| 10 ~ 15 | 6.57 | 6.35 |
| 15 ~ 20 | 5.54 | 6.95 |

**Fig. 13.** Distribution of fracture dissolution width under different acid injection periods.

progresses, the acid-rock reaction rate in each period is slowed down continuously, and the main increase in fracture width is decreased to 1.2-1.4, 1.0-1.2 and 0.8-1.0 mm, accounting for 75.53%, 84.32% and 88.52%, respectively.

The calculation of multidimensional roughness parameters reveals that the S_a and S_q exhibit a progressive increasing trend with the injection time increasing (Figs. 14(a)-14(b)). This indicates that the height undulations of the fracture surface become more intense. The S_{sk} and S_{ku} exhibit a trend of first decreasing rapidly and then increasing slowly (Figs. 14(c)-14(d)), which indicates that in the early stage of acid injection, the acid exhibits a relatively fast acid-rock reaction rate in the high convex peak areas. As a result, the height and number of convex peaks are decreased rapidly and the surface height distribution is caused to concentrate toward the median value. With the injection time further increasing, the height and number of convex peaks on the fracture wall surfaces gradually become stable. The S_{dr} exhibits a trend of first increasing rapidly and then decreasing slowly (Fig. 14(e)). This indicates that in the early stage of acid injection, the degree of unevenness (concavities and convexities) on the fracture surface is increased, which results in the fracture surface area being increased rapidly. However, with the injection time further increasing, the unevenness of the fracture surface is weakened gradually. The D exhibits a trend of first increasing, then decreasing, and finally tending to stabilize (Fig. 14(f)). This indicates that in the early stage of acid injection, the complexity of the fracture surface is increased. With the injection time further increasing, the complexity of the fracture surface tends to stabilize.

The reasons for such changes in these roughness parameters are analyzed as follows: In the early stage of acid injection, the acid-rock reaction rate is relatively fast and the reaction is prioritized to occur in the convex areas on the wall surfaces. This causes the roughness height parameters (S_a , S_q) to be rapidly increased and the microstructural development degree (S_{dr}) to be significantly improved. With the injection time increasing, the fracture width is gradually expanded, which causes the shear rate to decrease along with the acid-rock reaction rate, thus the variation range of all roughness parameters is decreased. Furthermore, the non-uniform etching capacity of the acid is gradually weakened, the convex peaks are gradually flattened, and S_{sk} tends toward a symmetric distribution. During the acid injection process, although the roughness parameters of the fracture surfaces on both sides exhibit a consistent changing trend, their variation ranges have obvious differences. This phenomenon also reflects that a differential dissolution of the acid is found to exist on both sides of the fracture surfaces.

6. Conclusions

In this work, a 3D numerical model of acid etching fracture was developed by coupling the acid-rock reaction model with computational fluid dynamics methods, which comprehensively incorporates the rheological property of acid and fracture surface roughness. The accuracy of the numerical simulation was verified through acid-etched fracture experiments, with a deviation of 11.15% in dissolved mass and errors within 10.00% for most roughness parameters. The numerical model was employed to investigate two primary aspects: The quantitative effect of the rheological index on acid flow, and the spatiotemporal evolution of acid flow and dissolution behaviors during acid fracturing. The results are summarized as follows:

- 1) The rheological properties of acid have a significant impact on its flow and dissolution behaviors within fractures. As the rheological index (n) increases, the average shear rate of the acid is decreased, while its apparent viscosity is increased exponentially. Concurrently, the average acid-rock reaction rate, fracture width after acid etching, and dissolution width are all decreased exponentially, and the degree of non-uniform etching on the fracture surface is weakened. The increase in fracture surface roughness after acid etching and the difference in roughness between the two fracture surfaces are both decreased as n increases.
- 2) The flow and dissolution behaviors of acid in fractures exhibit distinct spatiotemporal dynamics. During acid fracturing, the apparent viscosity of the acid and the acid-rock reaction rate are decreased exponentially, and the average fracture width is increased logarithmically with time. At the early stage of acid injection, the rapid expansion of fracture width is attributed to the relatively low apparent viscosity and high reaction rate of the acid. As the fracture widens, the velocity gradient of acid flow diminishes, leading to a reduction in the shear rate, a rise in apparent viscosity, and a subsequent decline in

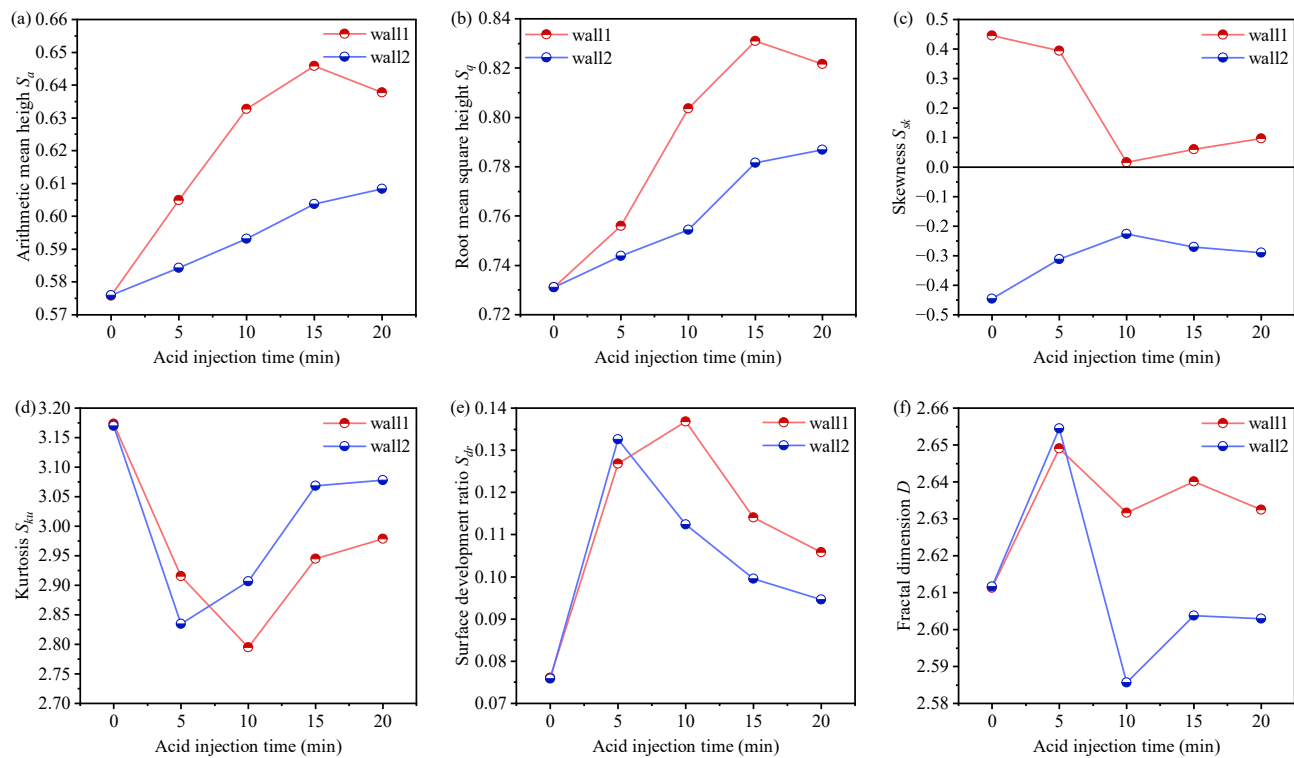


Fig. 14. Roughness parameters of acid-etched fracture surfaces under different acid injection times: (a) Arithmetic mean height S_a , (b) root mean square height S_q , (c) skewness S_{sk} , (d) kurtosis S_{ku} , (e) surface development ratio S_{dr} and (f) fractal dimension D .

the acid-rock reaction rate. As a result, the non-uniform etching capacity of the acid is weakened.

This work provides a feasible method for numerical simulation studies on the flow of acids with power-law characteristics in 3D rough fractures, offering theoretical support for optimizing acid fracturing parameters (such as fluid rheology, injection rate, and treatment duration) and improving stimulation outcomes in carbonate reservoirs. Future research will further enhance the model by incorporating the effects of heat and CO_2 generated by the acid-rock reaction, aiming to develop a more comprehensive representation of reactive transport. In addition, the acid-rock reaction rate model can be compiled into a user-defined function, which can be loaded into finite element simulation software to achieve improvable and flexible numerical simulation of acid flow and reaction in 3D rough fractures.

Acknowledgements

This research was funded by the National Natural Science Foundation of China (No. 21974014). We would also like to thank the College of Energy (College of Modern Shale Gas Industry) of Chengdu University of Technology and the State Key Laboratory of Oil and Gas Reservoir Geology and Exploitation for providing equipment support.

Supplementary file

<https://doi.org/10.46690/ager.2025.09.05>

Conflict of interest

The authors declare no competing interest.

Open Access This article is distributed under the terms and conditions of the Creative Commons Attribution (CC BY-NC-ND) license, which permits unrestricted use, distribution, and reproduction in any medium, provided the original work is properly cited.

References

- Abdelgawad, K. Z., Mahmoud, M., Hussein, I. Stimulation of high temperature carbonate gas reservoirs using seawater and chelating agents: Reaction kinetics. *Journal of Natural Gas Science and Engineering*, 2018, 55: 595-605.
- Afsar, H., Samadi, F., Esmailzadeh, F., et al. 3-d numerical simulation of sandstone matrix acidizing by non-newtonian fluid. *Journal of Petroleum Science and Engineering*, 2022, 208: 109666.
- Alhubail, M. M., Misra, A., Barati, R. A novel acid transport model with robust finite element discretization. Paper SPE188030 Presented at SPE Kingdom of Saudi Arabia Annual Technical Symposium and Exhibition, Dammam, Saudi Arabia, 24-27 April, 2017.
- Aljawad, M. S., Schwalbert, M. P., Zhu, D., et al. Improving acid fracture design in dolomite formations utilizing a fully integrated acid fracture model. *Journal of Petroleum Science and Engineering*, 2020, 184: 106481.
- Al-Shargabi, M., Davoodi, S., Wood, D. A., et al. A critical review of self-diverting acid treatments applied to car-

- bonate oil and gas reservoirs. *Petroleum Science*, 2023, 20(2): 922-950.
- Barboza, R. P., Schwalbert, M. P., Favero, J. L., et al. Modeling and simulation of the carbonate reactive-dissolution process by viscoelastic-surfactant-based acid. *Journal of Petroleum Science and Engineering*, 2022, 215: 110595.
- Bird, R. B., Stewart, W. E., Lightfoot, E. N. *Transport phenomena*, revised 2nd edition. Hoboken, USA, John Wiley & Sons, 2006.
- Chen, Y., Mao, H., Nie, W., et al. Investigation of nonlinear flow behavior along a rough-walled limestone fracture with acid dissolution. *Rock Mechanics and Rock Engineering*, 2024, 57(5): 3355-3369.
- Deng, Y., Yang, Y., Yang, T. Three systems of the oil and gas formation in the world. *Petroleum Research*, 2025, 10(1): 1-27.
- Dong, C., Zhu, D., Hill, A. D. Modeling of the acidizing process in naturally fractured carbonates. *SPE Journal*, 2002, 7(4): 400-408.
- Guo, J., Gou, B., Qin, N., et al. An innovative concept on deep carbonate reservoir stimulation: Three-dimensional acid fracturing technology. *Natural Gas Industry B*, 2020, 7(5): 484-497.
- Gou, B., Qin, N., Wang, C., et al. Acidizing model to couple the closure stress and acid-rock reactive transport in naturally fractured carbonate reservoir. Paper ARMA 20211221 Presented at 55th U.S. Rock Mechanics/Geomechanics Symposium, Virtual, 18-25 June, 2021.
- HaghaniGalougahi, M. Pore-scale simulation of calcite matrix acidizing with hydrochloric acid. *SPE Journal*, 2021, 26(2): 653-666.
- Huang, Z., Xing, H., Zhou, X., et al. Numerical study of vug effects on acid-rock reactive flow in carbonate reservoirs. *Advances in Geo-Energy Research*, 2020, 4(4): 448-459.
- Ivanishin, I., Kotb, A., Nasr-El-Din, H. A. Turbulence leads to overestimation of the acid-diffusion coefficient at typical experimental conditions using the rotating disk apparatus. *Journal of Petroleum Science and Engineering*, 2021, 205: 108805.
- Ignatenko, E. V., Bryanskaya, Y. V. Velocity distribution in channels of various geometry and roughness. *Power Technology and Engineering*, 2023, 57(3): 412-414.
- Jiang, Q., Yang, X., Gong, F. Development and evaluation of high temperature resistant cross-linked acid fracturing fluid system. *Chemical Industry and Engineering*, 2022, 39(1): 51-57.
- Kadafur, I. B., Aljawad, M. S., Mahmoud, M. Review of acid diffusion measurement methods in porous media. *Energy & Fuels*, 2020, 34(10): 11916-11941.
- Karayel, G. K., Javani, N., Dincer, I. Effective use of geothermal energy for hydrogen production: A comprehensive application. *Energy*, 2022, 249: 123597.
- Kong, X., Liu, B., Wan, X., et al. Experimental evaluation and optimization of improved conductivity of gelling acid etched fractures in deep, low-permeability reservoirs. *Fuel*, 2023, 348: 128468.
- Kotb, A., Ezzat, A. A., Ali, M., et al. A calibrated computational fluid dynamics model for simulating the rotating disk apparatus. *SPE Journal*, 2021, 26(6): 4022-4036.
- Kumar, U., Panda, D., Biswas, K. G. Augmented mass transfer in liquid-liquid flow through microchannels of different geometries. *Chemical Engineering and Processing-Process Intensification*, 2019, 137: 72-79.
- Lavrov, A. Redirection and channelization of power-law fluid flow in a rough-walled fracture. *Chemical Engineering Science*, 2013, 99: 81-88.
- Li, H., Shi, Y. Synthesis and performance of temperature- and acid-resistant ternary-copolymer thickener. *Materials Chemistry and Physics*, 2022, 292: 126866.
- Li, Q., Yi, X., Lu, Y., et al. The law of the hydrogen ion diffusion coefficient in acid rock reaction. *Journal of Petroleum Science and Engineering*, 2016, 146: 694-701.
- Ling, X., Yu, H., Qing, Y., et al. Acid fracturing: A perspective. *International Journal of Earth Sciences Knowledge and Applications*, 2024, 6(3): 397-400.
- Liu, P., Hu, H., Chen, X., et al. The influencing parameters and improve methods of acid-etched fracture conductivity: A review. *Geoenergy Science and Engineering*, 2024, 238: 212844.
- Liu, P., Kong, X., Feng, G., et al. Three-dimensional simulation of wormhole propagation in fractured-vuggy carbonate rocks during acidization. *Advances Geo-Energy Research*, 2023b, 7(3): 199-210.
- Liu, X., Li, Q., Li, N., et al. Numerical simulation of acid flow in rough fractures. *SPE Journal*, 2025a, 30(5): 3009-3028.
- Liu, Z., Qi, N., Jiang, P., et al. Developments of acid fracturing technology for enhanced geothermal systems: A review. *Applied Energy*, 2025b, 388: 125650.
- Liu, J., Zhao, J., Qin, S., et al. Research and application of acid fracturing stimulation mechanism in ultra-deep subsalt dolomite reservoir in tarim basin. *Journal of Petroleum Exploration and Production Technology*, 2023a, 13(3): 877-889.
- Lo, K. K., Dean, R. H. Modeling of acid fracturing. *SPE Production Engineering*, 1989, 4(2): 194-200.
- Maheshwari, P., Maxey, J., Balakotaiah, V. Reactive-dissolution modeling and experimental comparison of wormhole formation in carbonates with gelled and emulsified acids. *SPE Production & Operations*, 2016, 31(2): 103-119.
- Mehrabi, M., Fatemi Aghda, S. M., Sarkheil, H., et al. A systematic review to identify carbonate rock exploration paradigms and examine current and future research directions: A case study at one of the southwest oil fields of iran. *Journal of Petroleum Exploration and Production Technology*, 2025, 15(2): 34.
- Nasr-El-Din, H. A., Al-Mohammad, A. M., Al-Aamri, A. D., et al. Quantitative analysis of reaction-rate retardation in surfactant-based acids. *SPE Production & Operations*, 2009, 24(1): 107-116.
- Peng, J., Feng, R., Xue, M., et al. Research progress and engineering applications of viscous fluid mechanics. *Applied Sciences*, 2025, 15(1): 357.
- Romero, J., Gu, H., Gulrajani, S. N. 3D transport in acid-fracturing treatments: Theoretical development and con-

- sequences for hydrocarbon production. *SPE Production & Facilities*, 2001, 16(2): 122-130.
- Song, C., Lee, J. Reaction kinetics of an emulsified acid using a mixed emulsifier and carbonate rocks. *Colloids and Surfaces A: Physicochemical and Engineering Aspects*, 2023, 679: 132544.
- Subedi, J., Rajendran, S., Manglik, R. M. Laminar forced convection in viscous shear-thinning liquid flows inside circular pipes: Case for a modified power-law rheology. *Journal of Heat Transfer*, 2020, 142(12): 121802.
- Sui, Y., Cao, G., Tian, Y., et al. Application, progress, and trend of thickened acid fracturing in carbonate rock reservoir development. *Processes*, 2024, 12(10): 2269.
- Ugursal, A., Zhu, D., Hill, A. D. Development of acid fracturing model for naturally fractured reservoirs. *SPE Production & Operations*, 2019, 34(4): 735-748.
- van Domselaar, H. R., Schols, R. S., Visser, W. An analysis of the acidizing process in acid fracturing. *Society of Petroleum Engineers Journal*, 1973, 13(4): 239-250.
- Wang, P., Gou, Q., Zhang, B., et al. Application of 3d rough discrete fracture networks to fluid flow processes in fractured rock masses. *Geomechanics and Geophysics for Geo-Energy and Geo-Resources*, 2025a, 11(1): 23.
- Wang, S., Zhang, D., Guo, J., et al. Experiment and analysis of the reaction kinetics of temperature control viscosity acids with limestone. *Journal of Petroleum Science and Engineering*, 2018, 165: 305-312.
- Wang, S., Zhang, W., Gao, J., et al. Characteristics of shear thickening fluid and its application in engineering: A state-of-the-art review. *The International Journal of Advanced Manufacturing Technology*, 2024, 133(5): 1973-2000.
- Wang, X., Song, Y., Wu, P., et al. Rheological properties of hydroxypropyl guar gum fracturing fluids: Effects of cross-linking agents. *Carbohydrate Polymers*, 2025b, 366: 123837.
- Wang, Y., Fan, Y., Wang, T., et al. A new compound staged gelling acid fracturing method for ultra-deep horizontal wells. *Gels*, 2022, 8(7): 449.
- Williams, B. B., Nierode, D. E. Design of acid fracturing treatments. *Journal of Petroleum Technology*, 1972, 24(7): 849-859.
- Xu, D., Lei, H., Xiao, H., et al. Observation via particle image velocity (PIV) technology of seepage features in replicas of rock fractures. *Rock Mechanics and Rock Engineering*, 2024, 57(9): 6527-6541.
- Xu, S., Zhou, S., Zhou, J., et al. Multiscale pore structure evolution of longmaxi shale induced by acid treatment. *SPE Journal*, 2023, 28(2): 831-844.
- Yu, Y., Cui, J., Zhang, R., et al. Gelling acid thickener for oil and gas production: Preparation, properties and applications. *Oilfield Chemistry*, 2021, 38(3): 553-559. (in Chinese)
- Zeng, M., Zhou, H. Investigation of acid-etching evolution in natural fractures of carbonate reservoirs under high closure stress. *SPE Journal*, 2025, 30(1): 98-110.
- Zhang, Y., Kuang, J., Zhang, H., et al. Experimental study on the acid fracturing fracture propagation law of a fractured carbonate reservoir in the majiagou formation. *Processes*, 2025, 13(3): 695.
- Zhao, F., Jiao, X., Xia, X., et al. Evolution of rock pore structure and physical properties due to acidification: Recent advances and future perspectives. *Advances in Geo-Energy Research*, 2024, 14(3): 238-240.
- Zhao, M., Li, Y., Xu, Z., et al. Dynamic cross-linking mechanism of acid gel fracturing fluid. *Colloids and Surfaces A: Physicochemical and Engineering Aspects*, 2020, 607: 125471.
- Zhu, D., Wang, Y., Cui, M., et al. Acid system and stimulation efficiency of multistage acid fracturing in porous carbonate reservoirs. *Processes*, 2022, 10(9): 1883.
- Zhu, T., Zhang, Z., Liu, Z., et al. Simulation of hydraulic-mechanical-chemical coupled acid fracturing of rock with lattice bonds. *Heliyon*, 2024, 10(4): e26517.